J Mater Sci (2020) 55:8756–8767

Polymers & biopolymers

Fabrication and characterization of photonic cellulose nanocrystal films with structural colors covering full visible light

Guomin Zhao[1], Shuai Zhang[1], Shengcheng Zhai[1], and Mingzhu Pan[1,*]

[1] *College of Materials Science and Engineering, Co-Innovation Center of Efficient Processing and Utilization of Forest Resources, Nanjing Forestry University, Nanjing 210037, China*

Received: 7 February 2020
Accepted: 27 March 2020
Published online: 7 April 2020

ABSTRACT

Chiral nematic cellulose nanocrystal (CNC) photonic films with structure color were prepared by regulating the acid-to-pulp ratio (8:1, 10:1, and 12:1) and the hydrolysis temperature (45 °C and 60 °C). CNC prepared with a lower acid-to-pulp ratio and hydrolysis temperature obtained a higher aspect ratio, which made it easy for CNC to contact each other to produce chiral nematic structures and present iridescent film. The as-prepared CNC iridescent films can reflect natural light with a wavelength in the range of 360–695 nm. Consequently, the CNC films showed structural color of blue to orange, dependent on the acid hydrolysis conditions. The strategy presented herein paves the way for the simple and cost-efficient preparation of photonic materials with structural colors.

Introduction

Structural color, also called physical color, is a gloss caused by the wavelength of light. It is due to the existence of the fine structure of photonic nanomaterials with spatially ordered lattices, which exhibit brilliant colors of light to be refracted, diffusely reflected, diffracted, or interfered [1–3]. Structural colors are used in the field of smart sensors and optoelectronic functional materials due to their brilliant colors and structural controllability [4, 5]. Nevertheless, due to the lack of the inspirational designs of structures and efficient generation technologies of three-dimensional nanostructures, the development of the structural color is slow [6, 7].

In contrast, nature has created various excellent photonic materials with structure colors through the four and a half billion years of evolution and natural selection. The photonic materials are widespread in natural creatures [8, 9]. They appear as vivid structural colors that fascinate human beings. After a long period of evolution, the structural colors of the creatures in nature help them survive in the cruel natural laws of survival of the fittest [10]. For example, the *tortoise beetle* and *hercules beetle* alter their structural colors by varying an amount of water in the cuticle, to mislead their natural enemies [11, 12]. Some

Address correspondence to E-mail: mzpan@njfu.edu.cn

https://doi.org/10.1007/s10853-020-04616-4

nocturnal butterflies have a hexagonal photonic crystal array on their compound eye surface. These arrays can significantly suppress reflection loss while increasing the light transmittance at the interface over a wide wavelength range and a large field of view, which makes butterflies to adapt dark environment [8]. Similarly, a fish of *Paracheirodon innesi* normally displays a structural color of cyan, produced by periodically stacked microstructures of reflecting platelets in skin cells. Under urgent conditions, the blue color of the fish rapidly turns yellow due to the simultaneous change in the spacing of adjacent reflectors, thereby escaping the chasers [13].

Inspired by natural creatures, researchers have achieved great progress in developing photonic materials with structure color [14–17]. Recently, cellulose nanocrystal (CNC) has played an increasingly important role in the process of photonic materials with structure color. CNC, which is always derived from cellulosic materials, has a rod-shaped structural with 10 nm to 20 nm in diameter and several hundred nanometers in length [18], and it has high strength and modulus, high specific surface area, feasible modification, biocompatibility, and biodegradability [19–23]. Specially, CNC obtained by acid hydrolysis usually forms an equilibrium ordered chiral nematic phase due to sulfate ester groups on its surface [24–26]. Interestingly, the chiral nematic order makes CNC films display structural colors upon drying by evaporation-induced self-assembly (EISA) [27, 28]. Using CNC with the structural color as templates, researchers have synthesized a lot of artificial photonic materials. Cheung and coworkers have been generated the iridescent polymer composites with chiral nematic structures color by dispersing neutralized CNC in polar organic solvents such as DMF [29]. Shopsowitz and coworkers presented the formation of mesoporous silica and organosilica templated by the chiral nematic liquid crystal phase of CNC and then removed CNC from the composite films by calcination or acid hydrolysis to form chiral nematic mesoporous silica (CNMS) and organosilica with tunable pore diameters and structure color [30, 31]. Ana and coworkers assembled chiral plasmonic films with structure color by incorporating gold nanorods in CNC [32]. These CNC template photonic materials have brilliant structural colors. However, the high cost, low time efficiency, and some environmental pollution (such as organic solvents) still restricted developments for some advanced materials with structure color.

In previous studies [33], we found that the aspect ratio plays a crucial role in the formation and regulation of structural colors in CNC. The aspect ratio of CNC rods is predominantly determined by the acid hydrolysis conditions, which includes acid-to-pulp ratio, hydrolysis temperature, and hydrolysis time. However, few studies have addressed the influence of acid hydrolysis conditions on the structural colors of CNC during EISA process. Beck-Candanedo and coworkers prepared a CNC suspension from bleached kraft eucalyptus pulp and black spruce for 25 and 45 min., respectively. The two suspensions showed similar chiral nematic properties. A longer hydrolysis time produced a shorter, less polydisperse black spruce CNC, which slightly increased a critical concentration for the chiral nematic phase formation [34].

In this paper, a simple route to prepare the structural colors by imitating nature creatures is discussed. This study focuses on the regulation of structural colors of chiral nematic CNC iridescent films by the acid-to-pulp ratio (8:1, 10:1, and 12:1) and hydrolysis temperature (45 °C and 60 °C). The rod-shaped CNC with different aspect ratios was prepared by changing the acid-to-pulp ratio (8:1, 10:1, and 12:1) and hydrolysis temperature (45 °C and 60 °C). Subsequently, CNC suspensions were dried to form CNC iridescent films with different pitches during the EISA process. The as-prepared CNC iridescent films can reflect natural light with a wavelength in the range of 360–695 nm. Therefore, the CNC films showed structural color of blue to orange, which highlights a simple route to achieve regulation of structural colors in sensing materials.

Experimental

Materials

Microcrystalline cellulose (MCC) power (~ 50 μm in diameter) was provided by Shanhe Pharmaceutical Excipients Co., Ltd. (Anhui, China). H_2SO_4 (95–98 wt%), sodium chloride (NaCl ≥ 99.5 wt%), potassium chloride (KCl ≥ 99.5 wt%), and formaldehyde solution (HCHO: 37.0–40.0 wt%) at an analytical grade were obtained from Sinopharm Chemical Reagent Co., Ltd. (Nanjing, China).

Anhydrous potassium carbonate (K_2CO_3, ≥ 99.0 wt%) was purchased from Lingfeng Chemical Reagent Co., Ltd. (Shanghai, China). All chemical agents were used without further purification.

Preparation of CNC

Fifteen grams of MCC was hydrolyzed for 50 min. for preparation of the suspension. Hydrolysis was performed with 64 wt% sulfuric acid at acid-to-pulp ratios (weight ratio of the sulfuric acid to MCC) of 8:1, 10:1, and 12:1 at 45 °C and 60 °C, which is shown in Table 1. The suspension was then diluted tenfold to stop the reaction, then further diluted with the deionized water, and centrifuged for three cycles. The sample was placed inside dialysis membrane tubes (12,000–14,400 molecular weight cut-off, Biosharp, USA) and dialyzed against slow-running deionized water for 2 to 4 days until the pH of supernatant was neutral. Subsequently, the colloidal solution was dispersed by ultrasound treatment in an ultrasonic cell crusher (X-1200D, ATPIO, China) for 25 min. Finally, CNC suspension was condensed using a rotary evaporator (RE-501A, ATPIO, China) until the concentration of CNC reached 2.0 wt%.

Preparation of CNC iridescent films

CNC iridescent films were formed by casting the CNC suspension in polystyrene Petri dishes and allowing them to dry under ambient conditions (Fig. 1a), with typical thicknesses between 40 and 80 μm. Time-lapse photography of a CNC suspension during EISA shows the formation of chiral nematic ordering in the resulted free-standing film, with the structural color observed during the last 8–9 h (Fig. 1b).

Characterizations

Surface charge measurement

The zeta potential values of CNC colloid were measured by a Nano Zetasizer (Zetasizer Nano ZS, Malvern, UK) based on the principles of dynamic light scatting. A 4-mW laser source with a 633-nm wavelength was used as the light source. The suspension was diluted to 0.05 wt% and then sonicated with an ultrasonic bath (KQ-100DE, ATPIO, China) to obtain a homogeneous suspension before the measurement. The concentration of 0.05 wt% was within the proper range where the electric double layers on the cellulose particles barely overlapped with each other [35]. Each sample suspension was determined three times at 25 °C with a pH of 7.0.

Morphological analysis

The morphology of CNC colloids was observed with a transmission electron microscope (TEM, JEM-1400, JEOL, Japan) at 100 kV. Each sample suspension (0.05 wt%) was deposited onto carbon-coated grids (300-mesh copper) before measurement. The size distribution of CNC from TEM images was measured with the imaging MVS3000 software, and 50 particles were randomly taken for each sample. To further determine the chiral nematic arrangement of CNC films, the cross sections of CNC films were characterized by a field-emission scanning electron microscope (FE-SEM, HITACHI S4800, Thermo Scientific, USA). Samples were first fractured in liquid nitrogen and then coated with gold before examination at 15 kV.

Table 1 The zeta potential values and size distribution of CNC influenced by acid hydrolysis conditions

Samples	Acid-to-pulp ratio	Hydrolysis temperature (°C)	Zeta potential (mV)	Diameter (*D*, nm)			Length (*L*, nm)			Aspect ratio (*L*/*D*)
				Min.	Max.	Ave.	Min.	Max.	Ave.	
CNC-1	8:1	45	− 40.3	12.0	20.5	15.7	150.1	405.6	265.7	17.0
CNC-2	8:1	60	− 43.1	14.5	24.9	18.9	116.2	309.5	225.3	11.9
CNC-3	10:1	45	− 47.3	18.0	30.0	24.9	144.3	321.1	230.8	9.3
CNC-4	10:1	60	− 48.6	12.3	20.0	16.3	63.9	145.8	94.6	5.8
CNC-5	12:1	45	− 53.1	11.9	17.2	13.1	51.5	98.2	79.5	6.1
CNC-6	12:1	60	− 55.1	10.0	12.9	11.8	20.0	53.0	30.7	2.6

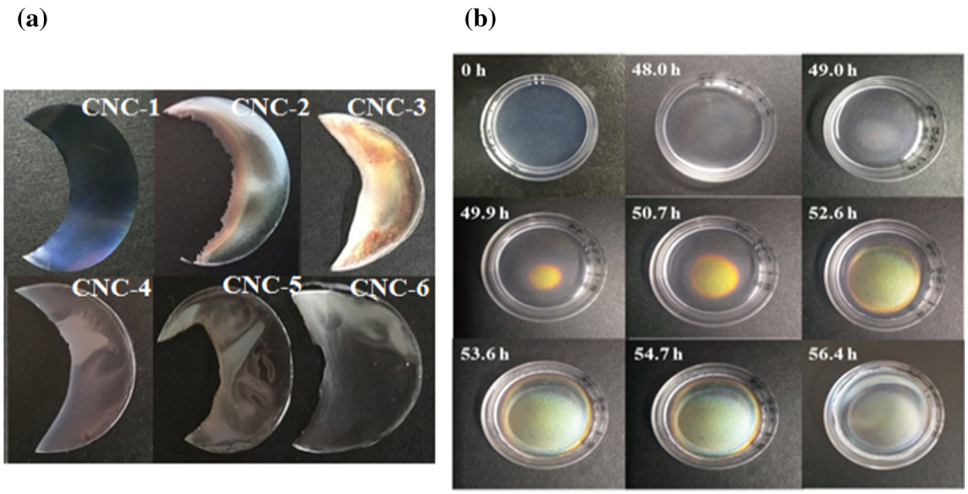

Figure 1 Preparation of the CNC iridescent films. **a** CNC iridescent films influenced with acid hydrolysis conditions. **b** Time-lapse photography of the EISA process for the CNC-1 iridescent film.

FTIR analysis

Fourier infrared (FTIR) spectra of CNC iridescent films were recorded by infrared spectrum instrument (Vertex 80, Bruker, Germany). The spectra of chiral nematic CNC iridescent films were recorded within a range of 4000–400 cm^{-1} with a resolution of 0.5 cm^{-1}.

XRD analysis

X-ray diffraction (XRD) was performed to investigate the phase structure of chiral nematic CNC iridescent films. The samples were flatted into pellets between two glass slides and placed in an X-ray diffractometer (Ultima IV, Rigaku, Japan) with Cu Kα radiation (λ = 0.15406 nm), operating at 40 kV and 30 mA. The diffraction profile was detected by using a locked couple 2θ scan from 5 to 50°. The crystallinity index (*CrI*) of the samples was calculated according to Eq. (1) [36]:

$$\mathrm{CrI}(\%) = \frac{A_{\mathrm{total}} - A_{\mathrm{am}}}{A_{\mathrm{total}}} \times 100 \quad (1)$$

where A_{total} and A_{am}, respectively, represent the total area of the diffract gram and the area of the amorphous peak.

The crystal size was estimated using the Scherrer equation, and the peak fitting process of the diffraction profile for the Scherrer equation was done in Peak Fit v4.12, using a Lorentz distribution with major diffraction peak positions [37].

$$D_{\mathrm{hkl}} = \frac{0.9\lambda}{\beta_{1/2}\cos\theta} \quad (2)$$

where D_{hkl} is the crystal size perpendicular to the diffracting planes with Miller indices of hkl, λ is the wavelength of X-ray radiation (λ = 0.15406 nm), $\beta_{1/2}$ is the full width at half maximum (FWHM) of the diffraction peaks, and θ is the corresponding Bragg angle.

Chiral nematic liquid crystal behavior measurement

CNC suspensions were introduced into the flat capillary under the capillary force. One edge of the flat capillary was blocked with paraffin, and the other edge was not blocked to allow water to evaporate. The flat capillary was transferred into a stage and observed using a polarizing optical microscope (POM, BX41, Olympus, Japan). The water inside each sample was allowed to slowly evaporate from the flat capillary edge. The texture of liquid crystal phase was examined between a pair of crossed polarizers, and the pictures were taken with a digital camera.

UV–visible analysis

The maximal reflection wavelength of CNC iridescent films was measured by a UV–Vis spectrophotometer (Lambda 950, PE, USA). The UV–Vis absorption spectra of the samples were recorded within a range of 250–800 nm with a resolution of 0.08 nm. In this work, all measurements were performed at 25 °C.

Results and discussion

Zeta potential analysis

The zeta potential reflects the electrostatic interactions of CNC in a colloidal dispersion, and its corresponding zeta potential values are listed in Table 1. The zeta potential was − 40.3 mV, − 47.3 mV, and − 53.1 mV at 45 °C for CNC-1, CNC-3, and CNC-5, respectively, corresponding to an increase in the acid-to-pulp ratio. Comparably, the zeta potentials reached − 48.6 mV and − 55.1 mV at 60 °C for CNC-4 and CNC-6, respectively. This result revealed that a higher acid-to-pulp ratio and hydrolysis temperature can induce in more hydroxyl groups within the surface of CNC, thereby resulting in more sulfate ester groups [38], which was evidenced by $–OSO_3^-$ content (Table S1). The increased sulfate ester groups have a noticeably negative zeta potential, and it plays a key role in achieving the chiral nematic structures of CNC.

Morphology of CNC suspensions and iridescent films

Figure 2a–f shows the morphology of CNC suspensions affected by acid hydrolysis conditions, and the size distribution of CNC is presented in Table 1. CNC-1 was oriented horizontally with a "slim rod-shaped" structure (Fig. 2a) with an average length of 265.7 nm, diameter of 15.7 nm, and an aspect ratio of 17.0. Comparatively, the aspect ratio was 11.9 and 9.3 for CNC-2, and CNC-3, respectively. Meanwhile, both CNC-2 and CNC-3 exhibited an horizontal arrangement (Fig. 2b, c). The CNC changes from "slim rod-shaped" to "short rod-shaped," and they become a random arrangement by increasing the acid-to-pulp ratio from 8:1 to 10:1 and the hydrolysis temperature from 45 to 60 °C. Furthermore, the aspect ratio of CNC is significantly influenced by the acid-to-pulp ratio prior to the hydrolysis temperature.

Figure 2a′–f′ shows an oriented structure of CNC arranged in layers that is affected by acid hydrolysis conditions. The CNC-1 iridescent film helically rotated in a certain direction in each layer and showed layered structures with periodic spacing (Fig. 2a′). The rising distance of the CNC rotation (as shown in the length of the red arrow in Fig. 2a′) was approximately 500 nm, which referred to a pitch of the CNC-1 iridescent film. CNC-2 and CNC-3 were also helically arranged in layers with periodic spacing (Fig. 2b′, c′). With an increase in the acid-to-pulp ratio and hydrolysis temperature, the pitch of CNC-2 and CNC-3 iridescent films increased to 650 nm and 950 nm, respectively (as shown in the length of the red arrow in Fig. 2b′, c′). Noticeably, the acid-to-pulp ratio had a more significant improvement in the pitch of CNC compared to the hydrolysis temperature. With a progressive increase in the acid-to-pulp ratio and hydrolysis temperature, CNC-4 and CNC-5 iridescent films showed some disordered regions that remained as a portion of the periodic helical structure (Fig. 2d′, e′). However, a periodic helical structure disappeared in CNC-6 iridescent film (Fig. 2f′). CNC-6 had a smaller aspect ratio of 2.6 from TEM analysis, which probably made the crystals isotropic, leading to layers being stacked rather than showing a periodic structure that was helically arranged during the EISA process.

Structure analysis of CNC

The chemical structure of CNC films affected with acid hydrolysis conditions is shown in Fig. 3 by FTIR spectra. The peaks at 3318, 2895, and 1431 cm^{-1} were characteristic stretching vibrations of –OH, C–H, and $–CH_2$, respectively. The characteristic peak at 1315 cm^{-1} was assigned to out-of-plane wagging of $–CH_2$ [39]. The peaks at 1035 and 830 cm^{-1} attributed to stretching vibrations of –C–O and $–C_1–H$, respectively. All the above peaks were the characteristic peaks of cellulose, which were observed in all spectra. The peak around 1640 cm^{-1} in all spectra assigned to the O–H bending of adsorbed water [40]. Due to the strong hydrogen bonding between –OH of CNC and –OH of water, it is difficult to completely remove the water adsorbed in the CNC [41]. In addition, the appearance of the peaks at 1206 (enlarged in the red rectangle) and 826 cm^{-1} in all spectra was, respectively, the stretching vibrations of S=O and C–O–S in $–OSO_3^-$ [42].

Figure 4 shows XRD spectra of CNC films affected with acid hydrolysis conditions for crystalline structure. CNC-1, CNC-2, and CNC-3 exhibited typical cellulose *I* characteristic peaks at 2θ = 14.9° and 22.7° corresponding to (110) and (200) lattice plates [43, 44]. When comparing CNC-1, CNC-2, and CNC-3, the peaks at 2θ = 14.9° and 22.7° weakened, and a new peak at 2θ = 20.8° appeared, corresponding to (110)

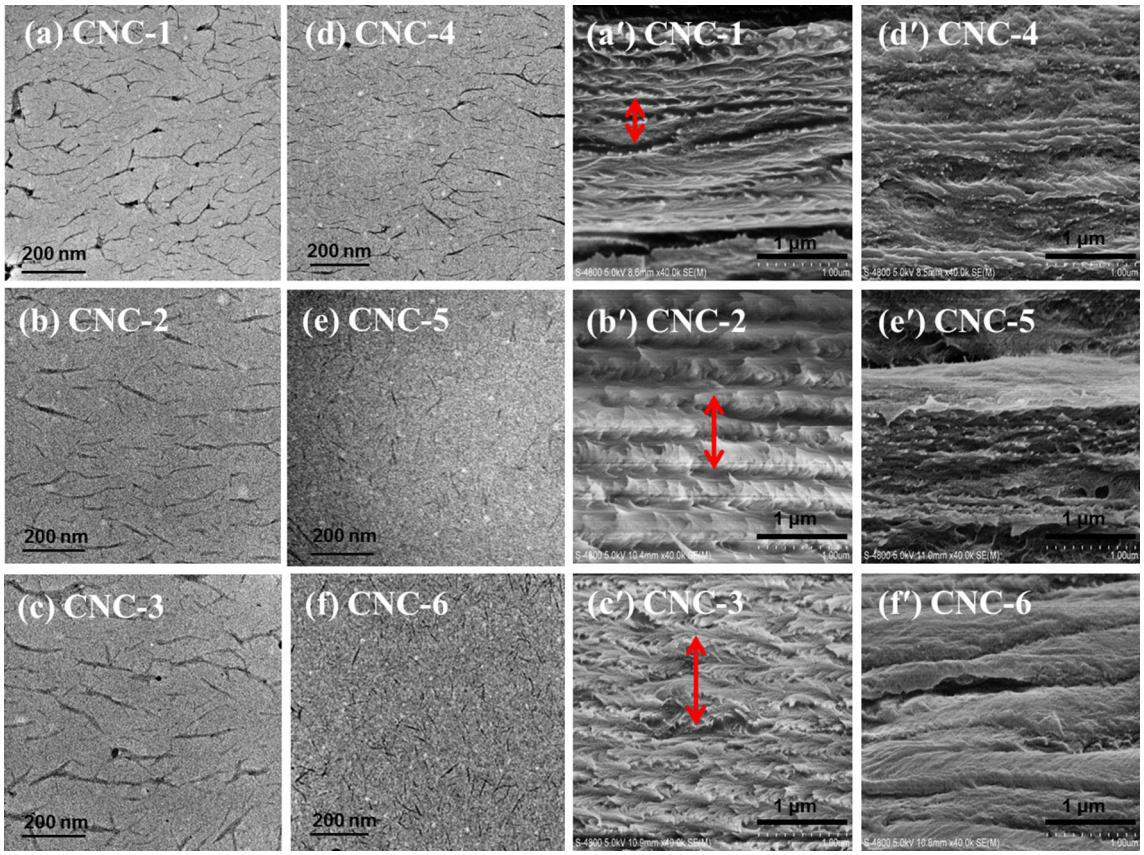

Figure 2 Morphology of CNC influenced with acid hydrolysis conditions: **a**–**f** TEM images of CNC suspensions, **a**′–**f**′ FE-SEM images of CNC iridescent films.

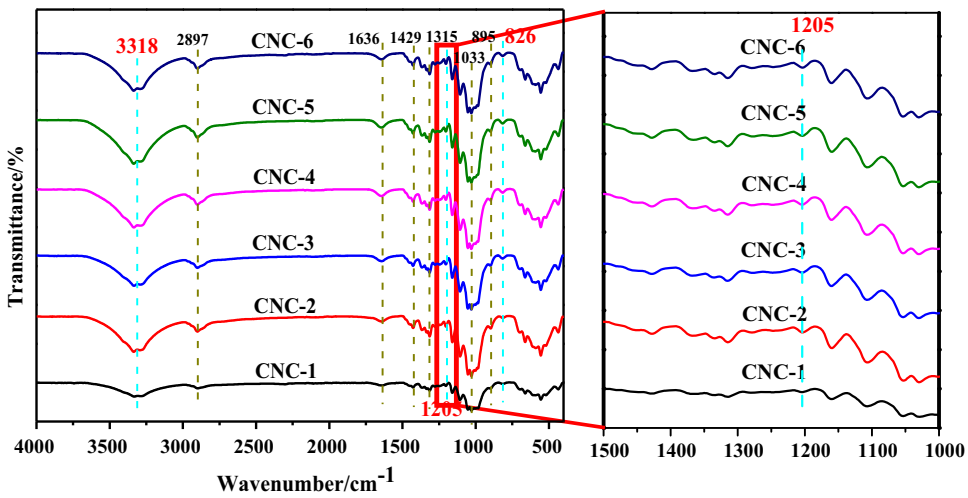

Figure 3 FTIR spectra of the CNC iridescent films influenced with acid hydrolysis conditions.

lattice planes of cellulose *II* with similar intensities for CNC-4, CNC-5, and CNC-6. Moreover, the minor peaks that appeared at 30.1° and 39.8° were attributed to (1–30) and (301) lattice planes of cellulose *II*, respectively [45]. A more severe acid hydrolysis condition likely disrupted the cellulose structure and destroyed the lattice planes of cellulose *I*, leading to an exposure of lattice planes of cellulose *II*. This finding was similar to that of a previous study conducted by Zoulikha and coworkers [46].

To further demonstrate the relationships between the crystal structure and the oriented structure of

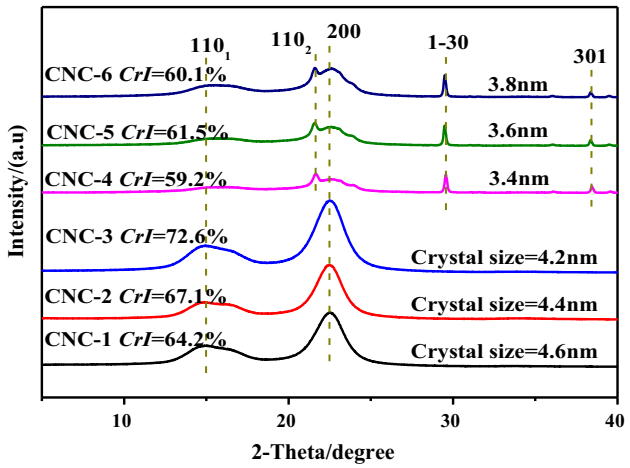

Figure 4 XRD spectra of the CNC iridescent films influenced by acid hydrolysis conditions.

CNC iridescent films, the *CrI* and crystal size of CNC films are calculated in Fig. 4. The *CrI* values of CNC-1, CNC-2, and CNC-3 were 64.2%, 67.1%, and 72.6%, respectively. The crystal sizes of CNC-1, CNC-2, and CNC-3 were 4.6 nm, 4.4 nm, and 4.2 nm, respectively. Combined with FE-SEM (Fig. 2a′–c′), the cross sections of the CNC-1, CNC-2, and CNC-3 iridescent films showed the periodic helical arrangement. In contrast, the *CrI* values of CNC-4, CNC-5, and CNC-6 decreased to 59.2%, 61.5%, and 60.1%, respectively, which were significantly lower than those of CNC-1, CNC-2, and CNC-3. Moreover, the crystal sizes of CNC-4, CNC-5, and CNC-6 were 3.4 nm, 3.6 nm, and 3.8 nm, respectively. The cross sections of the CNC-4, CNC-5, and CNC-6 iridescent films appeared to be a hybrid phase of the periodic helical and disordered arrangement (Fig. 2d′–f′). Thus, the CNC with single-crystal structure and high *CrI* may tend to be helically arranged and form layered structures with periodic spacing.

Chiral nematic liquid crystal behavior analysis

Figure 5 presents the formation process diagrams of the CNC liquid crystal phase. As an example of CNC-3, the rod-shaped CNC with an initial concentration of 2 wt% was dispersed in a flat capillary (as shown in the red circle in Fig. 5a). At this time, the suspension was isotropic. When the CNC concentration increased, the rod-shaped CNC gathered toward a lower end of the flat capillary, leading to the separation of an anisotropic phase, which then formed a weak liquid crystal phase at the critical concentration of 2.91 wt% after 20.2 h (Fig. 5b). Afterward, the CNC suspension was concentrated to 3.34 wt% after 24.5 h. The anisotropic phase and the liquid crystal phase increased at the lower end of the flat capillary, and the CNC suspension showed a birefringence phenomenon with a weakly striped texture (Fig. 5c). As water continued to evaporate, a substantial striped texture appeared in the CNC suspension when the suspension was concentrated to 3.72 wt% (Fig. 5d). When the concentration reached to 4.98 wt%, the striped textures contacted each other and then formed a fingerprint texture (as shown in the red circle in Fig. 5e). After 38.5 h, the concentration of CNC suspension was 5.56 wt%, and the volume and number of the fingerprint texture increased (as shown in the red circle in Fig. 5f); the liquid crystal in the fingerprint texture was arranged in a focal conical shape. This arrangement led to periodic changes in the optical refractive index, resulting in periodic birefringent extinction fringes in the fingerprint texture, which was similar to the behavior of CNC liquid crystal observed by Shopsowitz and coworkers [30]. At this time, the liquid crystal phase in the CNC suspension appeared as a chiral nematic liquid crystal. As the evaporation continued, the fingerprint texture continued to develop into colorful spheroids when the concentration was 9.36 wt% (Fig. 5g). As the concentration increased to 13.56 wt%, the colorful spheroids gathered in a fingerprint shape (arc shape) and formed a colorful pattern (Fig. 5h). This dynamic is attributed to favorably excluded volume interactions, resulting in higher packing entropy compared with the disordered phase, which drives the rod-shaped CNC nematic to be self-oriented [47]. After 48.5 h, the concentration was increased to 46.8 wt%, and the suspension exhibited a complete colorful pattern under crossed polarizers (Fig. 5i). At this time, the isotropic phase in the suspension was entirely converted to the anisotropic phase.

A comparison of POM diagrams of the chiral nematic liquid crystals of CNC is presented in Fig. 6. The isotropic phase was completely converted to the anisotropic phase when the concentration reached 36.7 wt% for CNC-1, and the blue pattern was presented under crossed polarizers (Fig. 6a). Comparatively, the phase transformation appeared at a concentration of 46.8 wt%, and the turquoise pattern was observed for CNC-2 (Fig. 6b). A higher

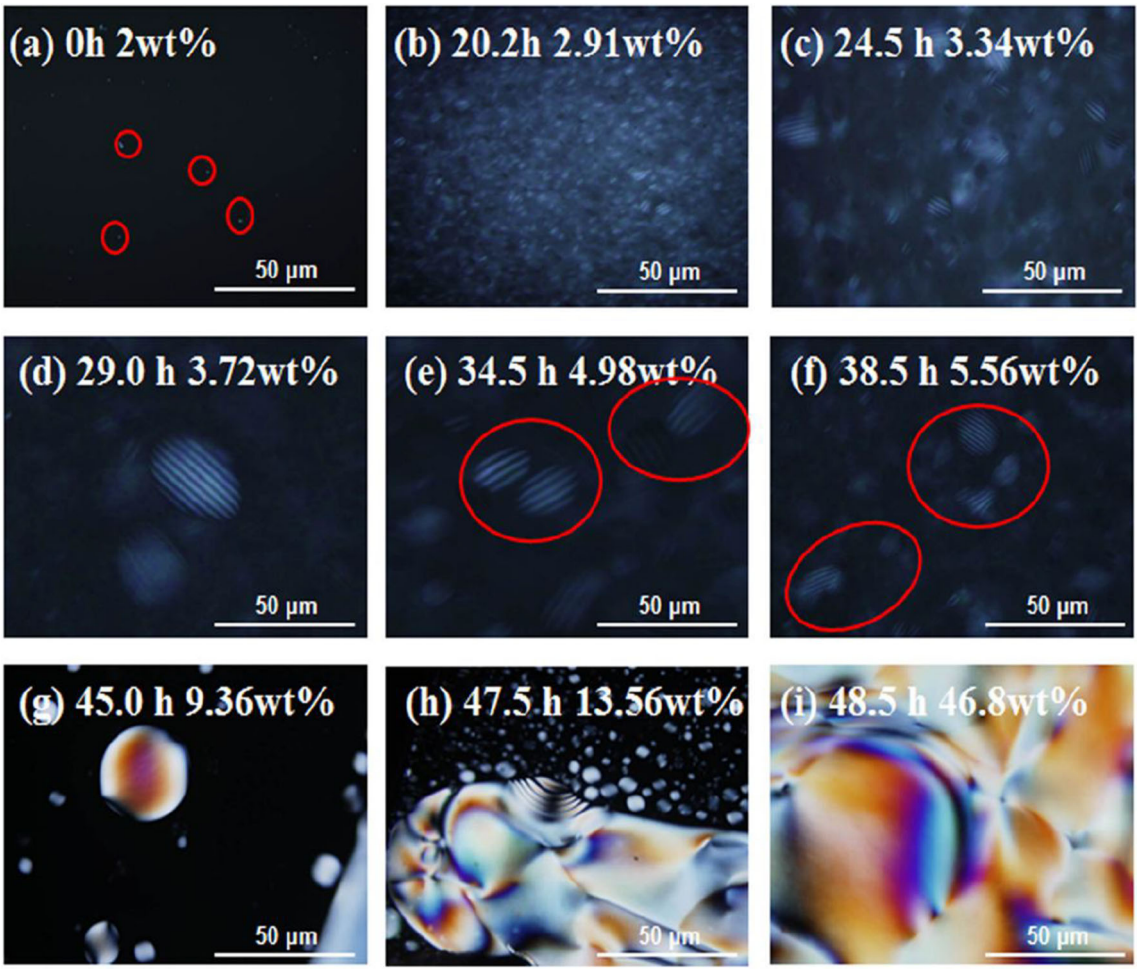

Figure 5 Formation process diagram of the CNC-3 liquid crystal phase.

hydrolysis temperature of 60 °C caused the anisotropic phase transformation, which was completed at the higher concentration of CNC suspension. Furthermore, the isotropic phase was completely converted to the anisotropic phase at a concentration of 50.4 wt%, and the orange pattern was present for CNC-3 (Fig. 6c). A higher acid-to-pulp ratio of 10:1 also induced a complete transformation of the anisotropic phase at the higher concentration of CNC suspension. Combined with the TEM results, the concentration for the CNC phase transition was negatively correlated with the aspect ratio. The CNC with a higher aspect ratio completely achieved the phase transition at a lower concentration. The higher aspect ratio for CNC likely limited the space for the stripe texture to develop; therefore, the CNC could easily contact each other to form a fingerprint texture. However, the suspension failed to form a colorful pattern under POM for CNC-4, CNC-5, and CNC-6 (Fig. 6d–f). This result indicated that the more severe acid hydrolysis could destroy the lattice planes of cellulose, and it had a negative influence on the phase transition of CNC.

UV–Vis analysis of CNC iridescent films

Figure 7 shows the UV–Vis absorbance spectra of CNC iridescent films. Clearly, the maximal reflection wavelengths appeared at 360 nm, 480 nm, and 695 nm and the iridescent films colors were violet, cyan, and orange for CNC-1, CNC-2, and CNC-3, respectively (Fig. 1a). The spectra of CNC films at different RH were transformed into a Commission on Illumination (CIE) chromaticity value, as shown in Fig. 7b; iridescent violet ($x = 0.1745$,$y = 0.006$), cyan ($x = 0.0995$, $y = 0.139$), and orange ($x = 0.7339$, $y = 0.2661$) were obtained for CNC-1, CNC-2, and CNC-3, respectively. This analysis indicated a higher

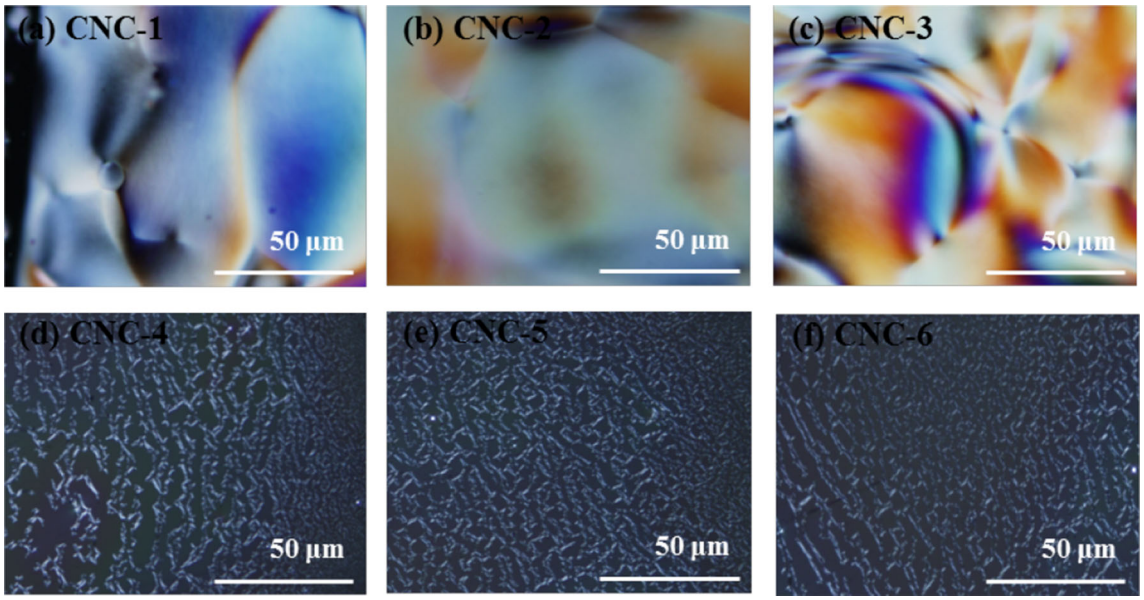

Figure 6 POM diagrams of the chiral nematic liquid crystal of CNC influenced by acid hydrolysis conditions.

acid-to-pulp ratio of 10:1, and hydrolysis temperature of 60 °C caused a redshift of the maximal reflection wavelength. Noticeably, the maximal reflection wavelength was absent in CNC-4, CNC-5, and CNC-6 due to a disappearance of the helical arrangement.

The maximal reflection wavelength of CNC films is related to the helical pitch within the CNC iridescent film during EISA. The maximal reflection wavelength (λ_{max}) can be described by the Bragg equation [Eq. (3)] and tuned by changing the pitch (P) or effective refractive index (n_{eff}) [48].

$$\lambda_{max} = n_{eff} P \sin \varphi \quad (3)$$

The formation of a helical arrangement of the chiral nematic liquid crystal phase caused the CNC film's iridescence during EISA of the CNC suspension; namely, the CNC iridescent film could reflect light of a wavelength equivalent to its P. Figure 8 illustrates the periodic helical structures of CNC affected by the acid-to-pulp ratio and hydrolysis temperature. CNC is arranged in a chiral nematic organization, with the rods mostly situated parallel to the films. Thus, the rising distance of each helically rotated layer is equivalent to the diameter of a single rod-shaped CNC. CNC-3 had a maximum diameter of 24.9 nm, leading to a maximum P, at the end of a periodic spiral rotation, which was consistent with the results of FE-SEM image (Fig. 2c′). Additionally, a larger crystal size of CNC-1 (Fig. 4) indicated a weak peak intensity of CNC-1 (Fig. 7a), which formed many

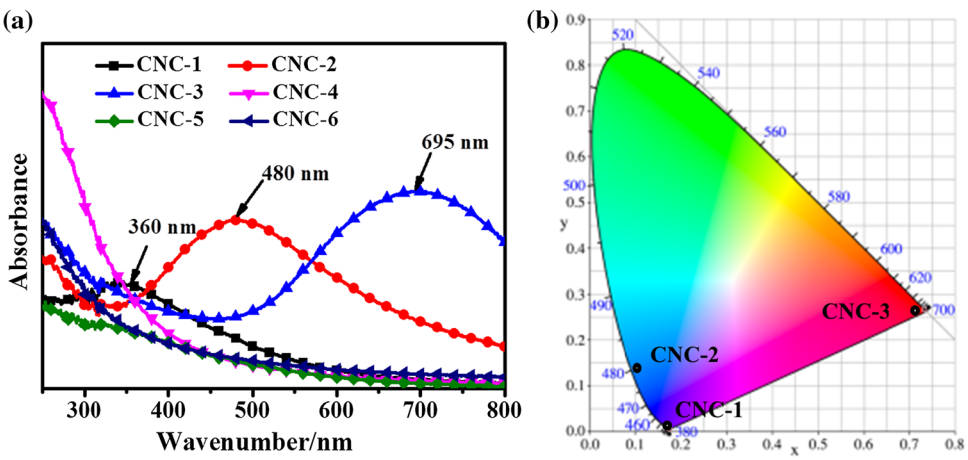

Figure 7 **a** UV–Vis absorbance spectra of the CNC iridescent films, **b** CIE chromaticity diagram of CNC films.

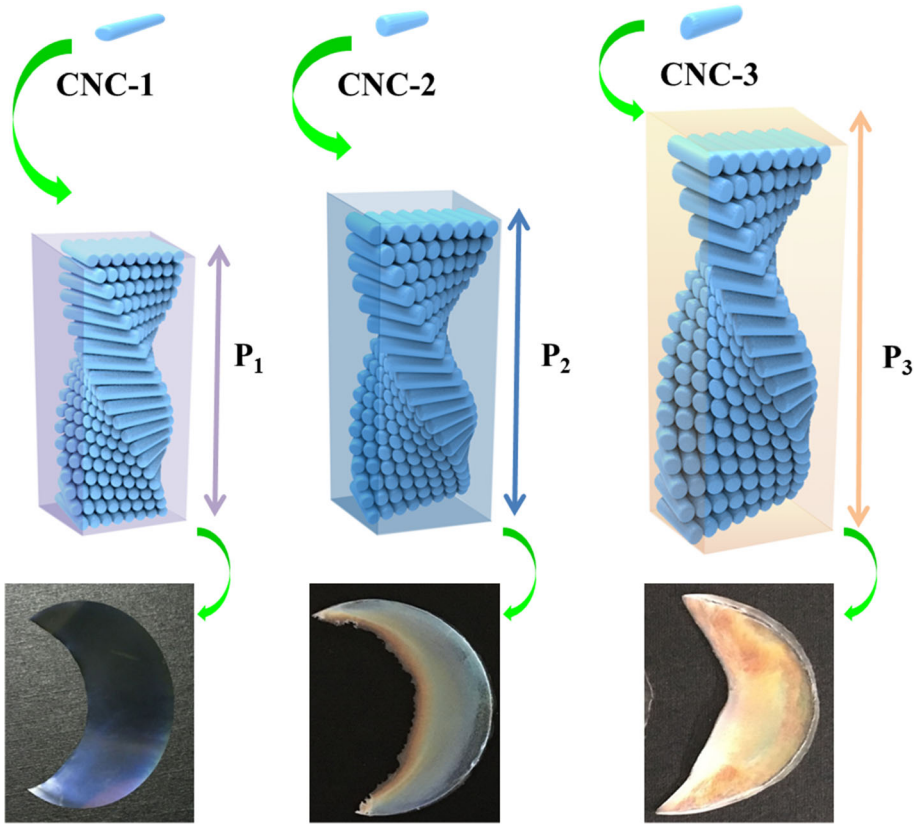

Figure 8 Possible schematic illustration of the structure color of CNC films influenced by acid hydrolysis conditions.

layers of rough surfaces in the chiral nematic structure of CNC-1. This dynamic may lead to a stronger diffused reflection of light from the crystals, resulting in a reduction in peak intensity, accounting for the lower n_{eff} of CNC-1 [49]. Consequently, λ_{max} of the CNC iridescent films was in an order of CNC-1 < CNC-2 < CNC-3, and the acid-to-pulp ratio had a more obvious effect on the λ_{max} of CNC than the hydrolysis temperature did.

Conclusions

Chiral nematic CNC films with structure color were presented by regulating the acid-to-pulp ratio and acid hydrolysis temperature. CNC was prepared with the lower acid-to-pulp ratio and the hydrolysis temperature obtained higher aspect ratio, which promoted CNC to attain a chiral nematic structure and present iridescent films. More specifically, the acid-to-pulp ratio had a more obvious effect than the hydrolysis temperature on the chiral nematic liquid crystal behavior and the structure of CNC iridescent films. The λ_{max} values of CNC-1, CNC-2, and CNC-3 were 360 nm, 480 nm, and 695 nm, respectively. In contrast, the more severe acid hydrolysis can destroy the lattice planes of cellulose, which played a negative influence on the formation of the chiral nematic structure of CNC. Consequently, the CNC films demonstrated structural color of blue to orange, which highlights a simple route to achieve regulation of structural colors in photonic materials.

Acknowledgements

This study was supported by the National Natural Science Foundation of China (Grant No. 31670556), the Science Fund for Distinguished Young Scholars of Nanjing Forestry University (Grant No. NLJQ2015-02), the Priority Academic Program Development of Jiangsu Higher Education Institutions (PAPD), the Postgraduate Research and Practice Innovation Program of Jiangsu Province (SJKY19_0895), the Key Laboratory of National Forestry and Grassland Bureau for Plant Fiber Functional Materials (Grant

No. 2019KFJJ06), and the Analysis and Testing Center of Nanjing Forestry University.

Compliance with ethical standards

Conflict of interest The authors declare no conflicts of interest.

Electronic supplementary material: The online version of this article (https://doi.org/10.1007/s10853-020-04616-4) contains supplementary material, which is available to authorized users.

References

[1] Bykov VP (1975) Spontaneous emission from a medium with a band spectrum. Quantum Electron 4:861–871

[2] Yablonovitch E (1987) Inhibited spontaneous emission in solid-state physics and electronics. Phys Rev Lett 58:2059–2062

[3] Johansen VE, Onelli OD, Steiner LM, Vignolini S (2017) Photonics in nature: from order to disorder. Funct Surf Biol III 3:53–89

[4] De LRR, Smith C (2000) Photonics. on the threshold of success. Nature 408:653–655

[5] Chandler CJ, Wilts BD, Brodie J, Vignolini S (2017) Structural color in marine algae. Adv Opt Mater 5:1600646

[6] Jacucci G, Bertolotti J, Vignolini S (2019) Role of anisotropy and refractive index in scattering and whiteness optimization. Adv Opt Mater 7:1900980

[7] Vignolini S, Rudall PJ, Rowland AV, Reed A, Moyroud E, Faden RB, Baumberg JJ, Glover BJ, Steiner U (2012) Pointillist structural colour in Pollia fruit. PNAS 109:15712–15715

[8] Vukusic P, Sambles JR (2003) Photonic structures in biology. Nature 424:852–855

[9] Parker AR, Townley HE (2007) Biomimetics of photonic nanostructures. Nat Nanotechnol 2:347–353

[10] Siddique RH, Vignolini S, Bartels C, Wacker I, Hölscher H (2016) Colour formation on the wings of the butterfly *Hypolimnas salmacis* by scale stacking. Sci Rep 6:36204

[11] Dong BQ, Liu F, Zi J, Liu XH, Zheng YM (2009) Structural color change in longhorn beetles Tmesisternus isabellae. Opt Express 17:16183–16191

[12] Vigneron JP, Pasteels JM, Windsor DM, Vertesy Z, Rassart M, Seldrum T, Dumont J, Deparis O, Lousse V, Biro LP, Ertz D, Welch V (2007) Switchable reflector in the Panamanian tortoise beetle Charidotella egregia (Chrysomelidae: Cassidinae). Phys Rev E 76:031907

[13] Lythgoe JN, Shand J (1989) The structural basis for iridescent color changes in dermal and corneal iridophores in fish. J Exp Biol 141:313–325

[14] Frka-Petesic B, Vignolini S (2019) So much more than paper. Nat Photonics 13:365–367

[15] Lopez C (2003) Materials aspects of photonic crystals. Adv Mater 15:1679–1704

[16] Aguirre CI, Reguera E, Stein A (2010) Tunable colors in opals and inverse opal photonic crystals. Adv Funct Mater 21:2565–2578

[17] Ge JP, Yin YD (2011) Responsive photonic crystals. Angew Chem 50:1492–1522

[18] Bondeson D, Mathew A, Oksman K (2006) Optimization of the isolation of nanocrystals from microcrystalline cellulose by acid hydrolysis. Cellulose 13:171–180

[19] Moon RJ, Martini A, Nairn J, Simonsen J, Youngblood J (2011) Cheminform abstract: cellulose nanomaterials review: structure, properties and nanocomposites. Chem Soc Rev 40:3941–3994

[20] Zhang JH, Xie SM, Zhang M, Zi M, He PG, Yuan LM (2014) Novel inorganic mesoporous material with chiral nematic structure derived from nanocrystalline cellulose for high-resolution gas chromatographic separations. Anal Chem 86:9595–9602

[21] Sacui IA, Nieuwendaal RC, Burnett DJ, Stranick SJ, Jorfi M, Weder C, Foster EJ, Olsson RT, Gilman JW (2014) Comparison of the properties of cellulose nanocrystals and cellulose nanofibrils isolated from bacteria, tunicate, and wood processed using acid, enzymatic, mechanical, and oxidative methods. ACS Appl Mater Interfaces 6:6127–6138

[22] Zhao GM, Ding CX, Pan MZ, Zhai SC (2018) Fabrication of NCC–SiO_2 hybrid colloids and its application on waterborne poly(acrylic acid) coatings. Prog Org Coat 122:88–95

[23] Chen CC, Wang HY, Li SY, Lu F, Li DA (2017) Reinforcement of cellulose nanofibers in polyacrylamide gels. Cellulose 24:5487–5493

[24] Revol JF, Bradford H, Giasson J, Marchessault RH, Gray DG (1992) Helicoidal self-ordering of cellulose microfibrils in aqueous suspension. Int J Biol 14:170–172

[25] Gray DG (2016) Recent advances in chiral nematic structure and iridescent color of cellulose nanocrystal films. Nanomaterials 6:213

[26] Araki J, Wada M, Kuga S, Okano T (2000) Birefringent glassy phase of a cellulose microcrystal suspension. Langmuir 16:2413–2415

[27] Lizundia E, Nguyen TD, Vilas JL, Hamad WY, Maclachlan MJ (2017) Chiroptical, morphological and conducting properties of chiral nematic mesoporous cellulose/polypyrrole composite films. J Mater Chem 5:19184–19194

[28] Liu P, Guo X, Nan FC, Duan YX, Zhang JM (2017) Modifying mechanical, optical properties and thermal processability of iridescent cellulose nanocrystal films using ionic liquid. ACS Appl Mater Interfaces 9:3085–3092

[29] Cheung CCY, Giese M, Kelly JA, Hamad WY, MacLachlan MJ (2013) Iridescent chiral nematic cellulose nanocrystal/polymer composites assembled in organic solvents. ACS Macro Lett 2:1016–1020

[30] Shopsowitz KE, Qi H, Hamad WY, Maclachlan MJ (2010) Free-standing mesoporous silica films with tunable chiral nematic structures. Nature 468:422–425

[31] Shopsowitz KE, Kelly JA, Hamad WY, Maclachlan MJ (2014) Biopolymer templated glass with a twist: controlling the chirality, porosity, and photonic properties of silica with cellulose nanocrystals. Adv Funct Mater 24:327–338

[32] Querejeta-Fernandez A, Chauve G, Methot M, Bouchard J, Kumacheva E (2014) Chiral plasmonic films formed by gold nanorods and cellulose nanocrystals. J Am Chem Soc 136:4788–4793

[33] Zhao GM, Du J, Chen WM, Chen DY (2019) Preparation and thermostability of cellulose nanocrystals and nanofibrils from two sources of biomass: rice straw and polar wood. Cellulose. https://doi.org/10.1007/s10570-019-02683-8

[34] Beckcandanedo S, Roman M, Gray DG (2005) Effect of reaction conditions on the properties and behavior of wood cellulose nanocrystal suspensions. Biomacromol 6:1048–1054

[35] Xing L, Gu J, Zhang WW, Tu DY, Hu CS (2018) Cellulose I and II nanocrystals produced by sulfuric acid hydrolysis of Tetra pak cellulose I. Carbohydr Polym 192:184–192

[36] Deepa B, Abraham E, Cordeiro N, Mozetic M, Mathew AP, Oksman K, Faria M, Thomas S, Pothan LA (2015) Utilization of various lignocellulosic biomass for the production of nanocellulose: a comparative study. Cellulose 22:1075–1090

[37] Uetani K, Yano H (2012) Zeta potential time dependence reveals the swelling dynamics of wood cellulose nanofibrils. Langmuir 28:818–827

[38] Han JQ, Zhou CJ, Wu YQ, Liu FY, Wu QL (2013) Self-assembling behavior of cellulose nanoparticles during freeze-drying: effect of suspension concentration, particle size, crystal structure, and surface charge. Biomacromolecules 14:1529–1540

[39] Kaushik A, Singh M (2011) Isolation and characterization of cellulose nanofibrils from wheat straw using steam explosion coupled with high shear homogenization. Carbohydr Res 346:76–85

[40] Johar N, Ahmad I, Dufresne A (2012) Extraction, preparation and characterization of cellulose fibres and nanocrystals from rice husk. Ind Crop Prod 37:93–99

[41] Moran JI, Alvarez VA, Cyras VP, Vazquez A (2008) Extraction of cellulose and preparation of nanocellulose from sisal fibers. Cellulose 15:149–159

[42] Lu P, Hsieh YL (2010) Preparation and properties of cellulose nanocrystals: rods, spheres, and network. Carbohydr Polym 82:329–336

[43] Savadekar NR, Mhaske ST (2012) Synthesis of nano cellulose fibers and effect on thermoplastics starch based films. Carbohydr Polym 89:146–151

[44] Giese M, Blusch LK, Khan MK, Hamad WY, Maclachlan MJ (2015) Responsive mesoporous photonic cellulose films by supramolecular cotemplating. Angew Chem Int Ed 126:8880–8884

[45] French AD (2014) Idealized powder diffraction patterns for cellulose polymorphs. Cellulose 21:885–896

[46] Zoulikha MR, Thierry M, Qiuyu ZJM, Nouviaire A, Sid-Ahmed R (2015) Combined steam-explosion toward vacuum and dilute-acid spraying of wheat straw. Impact of severity factor on enzymatic hydrolysis. Renew. Energ 78:516–526

[47] Habibi Y, Lucia LA, Rojas OJ (2010) Cellulose nanocrystals: chemistry, self-assembly, and applications. Chem Rev 110:3479–3500

[48] Hiltner PA, Krieger IM (1969) Diffraction of light by ordered suspensions. J Phys Chem 73:2386–2389

[49] Kumoda M, Watanabe M, Takeoka Y (2006) Preparations and optical properties of ordered arrays of submicron gel particles: interconnected state and trapped state. Langmuir 22:4403–4407